Desalination and Water Treatment
www.deswater.com

doi: 10.5004/dwt.2018.22792

129 (2018) 24–33
October

A novel method for calculating partition coefficient of saline water in direct contact membrane distillation: CFD simulation

Mohsen Hasanizadeh[a], Pooya Jafari[b], Saeed Shirazian[c,d,*]

[a]*Chemical Engineering Department, Amirkabir University of Technology, Tehran, Iran*
[b]*Department of Civil and Environmental Engineering, University of Houston, 4800 Calhoun St., Houston, TX 77204–4003, USA*
[c]*Department for Management of Science and Technology Development, Ton Duc Thang University, Ho Chi Minh City, Vietnam*
[d]*Faculty of Applied Sciences, Ton Duc Thang University, Ho Chi Minh City, Vietnam, email: saeed.shirazian@tdtu.edu.vn (S. Shirazian)*

Received 17 February 2017; Accepted 8 July 2018

ABSTRACT

For the first time, four different thermodynamic generic equations of state were applied to calculate the water partition coefficient in the polymeric direct contact membrane distillations studied in this research. Peng–Robinson equation of state was found to have the best fit with experimental data. Furthermore, the polymeric membrane performance was studied at different feed flow rate, temperature and cold stream flow rate. In addition, different feed and permeate flow directions were examined and as expected, cross-current flow arrangement showed the highest permeate flux.

Keywords: Partition coefficient; Desalination; Computational fluid dynamics (CFD); Direct contact membrane distillation (DCMD)

1. Introduction

Desalination is the process of removing salt from saline water solution to produce potable water. This process is used to reduce the shortage of potable water. Various techniques used for desalination process can be classified based on the applied driving force including pressure, temperature and electrical driving forces [1,2]. The multi-stage flash is among the temperature-driven processes which have been traditionally used while the reverse osmosis (RO) is a rather new membrane technique among the pressure-driven processes [2–7]. RO has increased the world's desalination capacity. Membrane distillation is a non-isothermal membrane process through which water is separated in the form of vapor from an aqueous saline solution [8]. Since a hydrophobic membrane is usually used in this process, water vapor can only pass through the membrane not the liquid [9,10]. The partial pressure difference between feed and permeate sides is the driving force for this process [11]. Therefore one of the MD advantages compared with RO and other desalination processes for the treatment of saline water is complete rejection of all non-volatile constituents in the feed solution; thus, almost 100% rejection of salty ions. The other advantage is due to the discontinuity of the aqueous phase across the membrane, water flux in MD is not influenced by the osmotic pressure gradient across the membrane [12]. Consequently, the greatest potential of MD can be realized through the treatment of highly saline solutions [13]. Duong et al. [14] have done a pilot study for the treatment of the RO brine from coal seam gas produced water by MD and they have concluded that fresh water recovery was increased from 75% to 95% when the RO was coupled with MD. In the other study, Martinetti et al. [15] showed that at low temperature, MD outperformed high-temperature MD and forward osmosis when treating a highly concentrated RO brine streams with lower scaling propensity but high total dissolved solid concentration.

Membrane distillation systems may be classified into four major groups based on permeate side conditions as follows [9,10,16]: (i) direct contact membrane distillation (DCMD), where the membrane directly comes into contact with

* Corresponding author.

different liquid streams (feed and permeate). In this method, the hot stream (feed) flows through one side of the membrane while the cold stream (permeate) flows through the other side; (ii) vacuum membrane distillation, where feed is introduced into one side of the membrane, the permeate side is under vacuum condition and the vapor passed through the membrane is brought to the condenser; (iii) sweeping gas membrane distillation (SGMD), where a sweep gas is used on the permeate side to transfer the water through membrane; and (iv) air gap membrane distillation (AGMD) where the feed is introduced into one side of membrane while a condensing surface exists on the other side and there is an air gap between the surface and the membrane, so the solvent vapor is collected on the condensing surface whereas it could be recovered.

Laganà et al. [17] investigated membrane behavior in a DCMD mode using computational fluid dynamics (CFD). They considered the effect of various properties of membrane morphology such as distribution of pores of different diameters, elasticity and other mechanical properties upon flux. Charfi et al. [18] presented a model to describe heat, mass and momentum transports through the three parts of a SGMD, namely: feed, membrane, and permeate side. Xu et al. [19] presented a model for the AGMD process of NaCl solution to predict heat and mass transfer behavior of the process. They found that temperature polarization phenomena can be reduced, and mass flux can be enhanced with increase in the feed Reynolds number.

Tang et al. [20] considered vacuum membrane distillation of NaCl aqueous solution. In their study, the permeate flux increased by increasing feed flow rate. Yu et al. [21] proposed a model to analyze heat and mass transfer in DCMD system. Based on the laminar flow assumption they found that Nusselt number was increased by increasing the feed Reynolds number.

To carry out design calculations of desalination modulus and comparing with obtained experimental data for industrial applications, a reliable mathematical model should be developed. The desired parameters that should be investigated are feed temperature, feed flow rate, and permeate flow rate. In this study, CFD approach is applied to describe the DCMD process of saline water. Various thermodynamic generic cubic equations of state were examined in order to compare which thermodynamic model best fits the experimental data. Moreover, different arrangements of cold and hot streams were investigated and the best arrangement exhibiting the highest permeate flux was determined. The experimental data of Shirazi et al. [8] was applied in this study. The governing equations (momentum, mass, and temperature) solved numerically to simulate the membrane performance in our previous study [22] were supplemented by applying generic cubic equations of state for calculation of partition coefficient of water between feed and membrane sections in this study. This method was shown to be successful in simulating the SGMD [23].

2. Model development

A schematic diagram of the membrane and flow directions considered in this study is shown in Fig. 1. A mathematical model is presented for vapor transfer through the membrane. The saline water enters at $y = 0$ and exits at $x = 0$, while the cold stream enters from the other side of the membrane at $y = L$ and exits at $x = x_3$ (the feed and the permeate move in a cross-current arrangement). This is a pressure-driven process in which the vapor penetrates from feed side toward the permeate side in x-direction due to the pressure gradient between feed and permeate. On the permeate side, pure cold water was used to collect the transferred water and the pure water was separated from saline water.

Temperature difference between the feed and permeate side supplies mass transfer driving force and the mass transfer process could be divided into three consecutive steps including: (i) selective absorption of permeate by membrane on the feed side, (ii) selective diffusion on the membrane side, and (iii) desorption to the permeate side (the other side of the membrane).

The following simplified assumptions were made to develop the model equations:

- Steady-state and isothermal conditions
- Constant and uniform velocity on permeate side
- Constant membrane temperature
- Laminar flow in the feed side
- 100% salt rejection (a rational assumption made due to experimental results [8])

2.1. Governing equations in the feed side

The mass transfer equation is used to describe water transfer from feed side to the permeate side which is expressed as follows [24]:

$$\frac{\partial C_w}{\partial t} + u\nabla C_w = \nabla(-D_w \nabla C_w) + R_w \tag{1}$$

where C_w is water concentration (mol/m^3), D_w is diffusion coefficient (m^2/s), u is velocity (m/s), t is time (s), and R_w is the reaction rate (mol/m^3 s), that is, zero in this study.

Based on the assumptions, the continuity equation for water in the feed side is simplified to the following equation:

$$D_{\mathrm{wf}}\left[\frac{\partial^2 C_{\mathrm{wf}}}{\partial x^2} + \frac{\partial^2 C_{\mathrm{wf}}}{\partial y^2}\right] = u_y \frac{\partial C_{\mathrm{wf}}}{\partial y} \tag{2}$$

with the boundary conditions of:

at $y = 0$: $C_{\mathrm{wf}} = C_0$
at $y = L$: $\partial C_{\mathrm{wf}}/\partial y = 0$
at $x = 0$: Convective flux
at $x = x_1$: $C_{\mathrm{wf}} = C_{\mathrm{wm}} \times m$

where m is water partition coefficient between feed and membrane which is calculated using appropriate thermodynamic cubic equations of state which the required parameters are summarized in Table 1. C_{wf} and D_{wf} are water concentration (mol/m^3) and diffusion coefficient (m^2/s) in feed side, respectively.

Moreover, the velocity distribution on the feed side should be obtained. It is expressed as the following equation [24]:

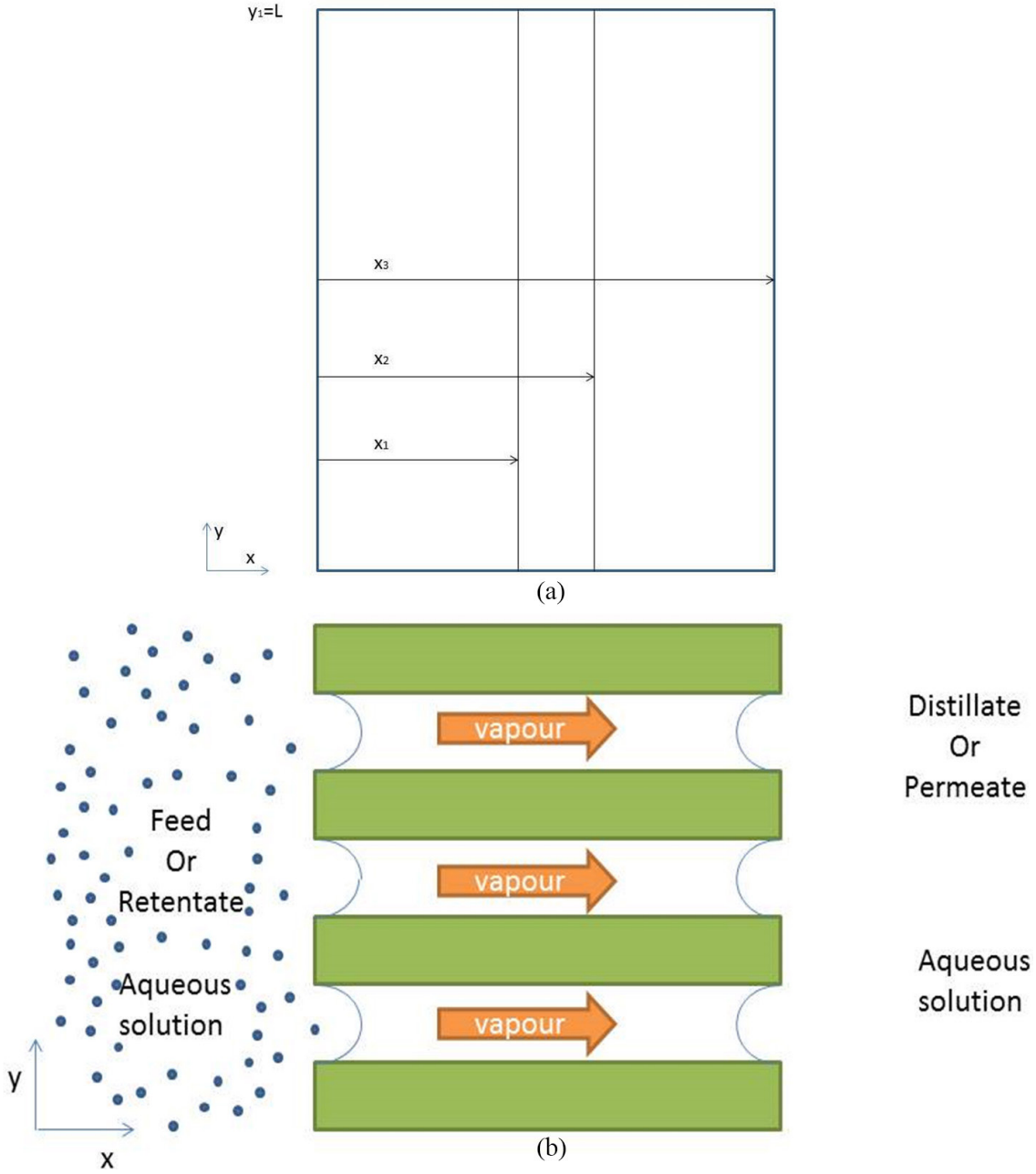

Fig. 1. Schematic diagram of (a) membrane and (b) flow directions.

Table 1
Parameter assignments for equations of state

Eq. of state	$\alpha(T_r)$	σ	ξ	Ω	ψ	Z_c
VdW(1873)	1	0	0	1/8	27/64	3/8
RK(1949)	$T_r^{-1/2}$	1	0	0.08664	0.42748	1/3
SRK	$\alpha_{SRK}(T_r, \omega)$	1	0	0.08664	0.42748	1/3
PR	$\alpha_{PR}(T_r, \omega)$	$1+\sqrt{2}$	$1-\sqrt{2}$	0.07779	0.45724	0.30740

$$\rho\frac{Du}{Dt} = -\nabla P + \mu\nabla^2 u + \rho g \tag{3}$$

where ρ is density (kg/m^3), P is pressure (Pa), μ is dynamic viscosity (Pa s), and g is gravity (m/s^2). Under steady-state and laminar flow conditions Eq. (3) is simplified to:

$$-\nabla P + \mu\nabla^2 u + \rho g = 0 \tag{4}$$

Appropriate boundary conditions for Eq. (4) include:

At $x = 0$: $P = P_{atm}$
At $x = x_1$ and $y = L$: $u_y = 0$
At $y = 0$: $u_y = u_0$

P_{atm} is atmospheric pressure (Pa) and u_0 is equal to inlet velocity (m/s).

Diffusion coefficient of water in saline water is determined from Wilke and Chang [25] equation (Eq. (5)). This empirical equation is used for diffusion of species in dilute solutions:

$$D_{ij}^{0} = \frac{7.4\times10^{-8}(\varphi M_j)^{1/2}T}{\mu_i v_i^{0.6}} \tag{5}$$

where D_{ij}^{0} is water diffusion coefficient in saline water (cm²/s), M_j is molecular weight of saline water (kg/kg mol), T is temperature (K), μ_i is viscosity of saline water (cp), v_i is molar volume of water (cm³/gmol), and ϕ is association factor of water accounting for hydrogen bonding.

2.2. Governing equations in the membrane side

The continuity equation for water transport in the membrane side is developed as follows:

$$D_{\mathrm{wm}}\left[\frac{\partial^2 C_{\mathrm{wm}}}{\partial x^2}+\frac{\partial^2 C_{\mathrm{wm}}}{\partial y^2}\right]=0 \tag{6}$$

where the diffusion coefficient D_{wm} is calculated from the following equation [26]:

$$D_{\mathrm{wm}} = 48.5 d_{\mathrm{pore}}\left(\frac{T}{M}\right)^{1/2} \tag{7}$$

C_{wm} and D_{wm} are water concentration (mol/m³) and diffusion coefficient within membrane (m²/s), respectively. M is molecular weight of water (kg/kg mol), T is temperature (K) and d_{pore} is pore diameter in the membrane (m).

The effective diffusion coefficient in membrane (D_{eff}) is calculated from the following equation:

$$D_{eff} = \varepsilon_p \frac{D}{\tau} \tag{8}$$

where ε_p and τ are porosity and tortuosity of the membrane, respectively.

The appropriate boundary conditions for using in Eq. (6) include the following:

At $x = x_1$: $C_{\mathrm{wm}} = C_{\mathrm{wf}}/m$
At $x = x_2$: $C_{\mathrm{wm}} = C_{\mathrm{wp}}$
At $y = 0$: $\partial C_{\mathrm{wm}}/\partial y = 0$ (insulation boundary)
At $y = L$: $\partial C_{\mathrm{wm}}/\partial y = 0$ (insulation boundary)

2.3. Governing equations in the permeate side

The mass balance equation for permeate is expressed as:

$$D_{wp}\left[\frac{\partial^2 C_{wp}}{\partial x^2}+\frac{\partial^2 C_{wp}}{\partial y^2}\right] = u_y \frac{\partial C_{wp}}{\partial y} \tag{9}$$

where C_{wp} and D_{wp} are water concentration (mol/m³) and diffusion coefficient in the permeate side (m²/s), respectively. The diffusion coefficient (D_{wp}) in the permeate side is calculated from Eq. (5).

The boundary conditions for using in Eq. (9) include:

At $x = x_2$: $C_{\mathrm{wp}} = C_{\mathrm{wm}}$
At $x = x_3$: Convective flux
At $y = 0$: $\partial C_{\mathrm{wp}}/\partial y = 0$ (insulation boundary)
At $y = L$: $C_{\mathrm{wp}} = 0$

2.4. Determining partition coefficient (m)

In order to calculate the partition coefficient which relates the water concentration in the liquid and vapor phase near the membrane, compressibility factor of water in the liquid phase (Z_l) and compressibility factor of water in the vapor phase (Z_v) should be estimated first. Vapor and vapor-like, and liquid and liquid-like roots of the generic cubic equations of state were used to calculate these quantities which in turn, yielded to estimation of partition coefficient (a ratio of Z_v to Z_l). Z_v can be calculated as [27]:

$$Z_v = 1+\beta-q\beta\left(\frac{Z-\beta}{(Z+\varepsilon\beta)(Z+\sigma\beta)}\right) \tag{10}$$

where β and q are dimensionless constants which can be calculated as follows:

$$\beta = \Omega\frac{P_r}{T_r} \tag{11}$$

$$q = \frac{\psi\alpha(T_r)}{\Omega T_r} \tag{12}$$

T_r and P_r are reduced temperature and reduced pressure, respectively. ε, σ, Ω, Ψ and $\alpha(T_r)$ are other dimensionless constants.

Z_l can be estimated as:

$$Z_l = \beta+(Z+\varepsilon\beta)(Z+\sigma\beta)\left(\frac{1+\beta-Z}{q\beta}\right) \tag{13}$$

The used coefficients for Eqs. (10)–(13) are listed in Table 1.

The value of α for SRK and PR equations can be obtained as a function of reduced temperature and acentric factor (ω) by the following relations [27]:

$$\alpha_{\mathrm{SRK}}(T_r,\omega) = \left[1+(0.480+1.574\omega-0.176\omega^2)(1-T_r^{1/2})\right]^2 \tag{14}$$

$$\alpha_{\mathrm{PR}}(T_r,\omega) = \left[1+(0.37446+1.54226\omega-0.26992\omega^2)(1-T_r^{1/2})\right]^2 \tag{15}$$

2.5. Numerical method

The governing equations with the introduced supplementary equations were solved together using the finite element scheme. The numerical solutions for governing equations were obtained using COMSOL Multiphysics software version 4.3a (1066MHz CPU speed, 4GB RAM). COMSOL produced elements in free triangular shape. According to the network independency results, a total of 5,581 meshes were applied in the simulation. The computational time for solving the set of equations was about 1 min. The algorithm used for the computations and the mesh produced by COMSOL are shown in Figs. 2 and 3. Also, the solver parameters and the mesh details used by COMSOL software are summarized in Table 2.

3. Results and discussion

The continuity and momentum equations were solved under various operating conditions on the feed and permeate sides of the PTFE, PP and PVDF membranes to evaluate the accuracy of the model. The simulated results were compared with experimental data [8]. In this model, the partition coefficient m was calculated using appropriate thermodynamic cubic equations of state. Equations of state used in this study were Peng–Robinson (PR), Redlich–Kwong (RK), Soave–Redlich–Kwong (SRK), and Van der Waals (VdW). The total error of simulated results by using different applied thermodynamics relations was calculated using Eq. (16) [28] and the results are shown in Table 3.

$$\text{Total error}(\%) = \frac{\sum J_{\text{exp}} - \sum J_{\text{sim}}}{\sum J_{\text{exp}}} \times 100 \tag{16}$$

where J is the flux of water (L/m^2 h).

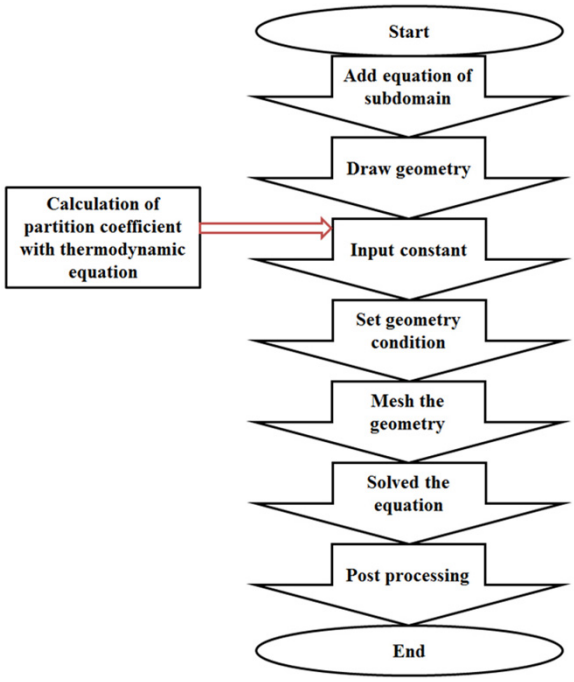

Fig. 2. A flowchart of the numerical optimization method.

According to Table 3, the Peng–Robinson model with minimal error exhibited the best fit for calculating the partition coefficient and modeling of the process while the Redlich–Kwong and Van der Waals had high errors when compared with experimental data. The total errors summarized in Table 3 are the average of errors for all membrane performances at different operating conditions. When these results using PR equation of state were compared with our

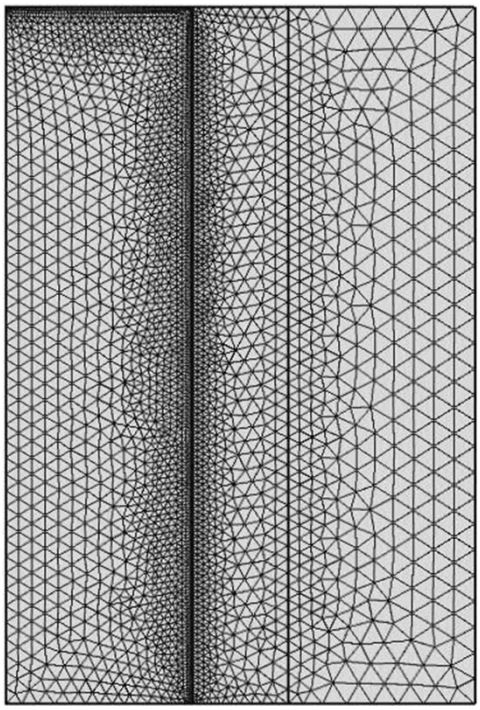

Fig. 3. Magnified segments of the mesh used in the numerical simulation (5,553 elements for the whole domain).

Table 2
Mesh details and solver's parameters used in this study

No. of degrees of freedom	28,616
No. of elements	5,581
Mesh shape	Free triangular
Solver	Stationary
Relative tolerance	3.0×10^{-6}
Maximum no. of iteration	8

Table 3
Total error of the obtained simulated data applying different cubic equations of state

Cubic equation of state	Total error (%)
VdW	108.83
RK	19.22
SRK	13.09
PR	0.06
Constant partial coefficient (previous study [22])	4.53

findings in our previous work [22], the deviation from modeled and experimental results was decreased significantly from 4.5% from our previous work to 0.06% for this work. While we had the best match of data with PR, the findings from the model which utilized VdW equations of state did not yield to promising results with deviation from experimental results of 108.83%. High accuracy of the PR and SRK cubic equations showed that they were developed specifically for vapor–liquid equilibrium calculations, in comparison with RK and VdW cubic equations. These findings were in a good agreement with findings from literature [27]. As shown in Fig. 4, permeate flux calculated by PR equation of state for three different membranes revealed better agreement with the experimental data in comparison with the other equations of state.

As it can be seen from Fig. 4, the PTFE had the highest flux among three studied membranes and PVDF achieved higher flux when compared with the PP membrane. These findings can be related to the membrane morphology and hydrophobicity. Hydrophobicity is one of the major characteristics in membrane distillation and high membrane hydrophobicity causes higher permeate flux and performance [29]. Based on the atomic force microscopy (AFM) images [8], PTFE membrane had higher contact angle in comparison with PVDF and PP membranes which consequently results in higher flux. From the scanning electron microscopy images of studied membranes [8], PVDF had non-uniform structure and larger gaps in it which yielded to higher flux than the PP membrane. In this study, the differences in the structure of membranes were studied due to the difference in the thickness and porosity of the membranes. However, our study lacks the effects due to the change in hydrophobicity.

3.1. Velocity distribution

The velocity of water vs. dimensionless length of the membrane (y/l) is shown in Fig. 5(a) for three different flow rates. The velocity field shown in Fig. 5(b) was solved and simulated using Navier–Stokes equations. From the profile, as saline water entered from bottom of the module and existed from the left side, the maximum velocity region was observed near the wall on the feed side entrance. The velocity decreased with decreasing the flow rate.

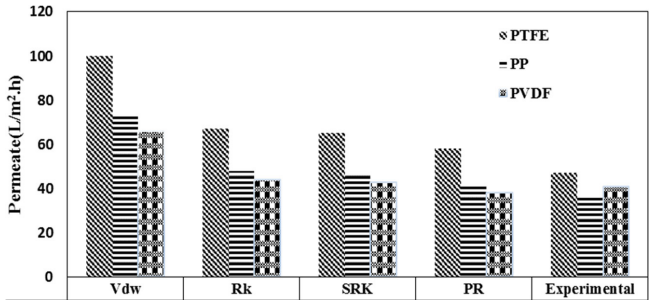

	Vdw	Rk	SRK	PR	Experimental
PTFE	100	67	65	58	47
PP	73	48	47	42	36
PVDF	66	44	43	38	41

Fig. 4. Permeate flux of the studied membranes by use of different equations of state (feed temperature = 80°C, cold stream temperature = 20°C, feed flow rate = 800 mL/min [0.12 m/s] and cold stream flow rate = 400 mL/min [0.06 m/s]).

3.2. Feed flow rate

The simulated results for PTFE porous membrane permeate flux are shown in Fig. 6 and is compared with experimental data for various feed flow rates from 400 to 800 mL/min. The method for calculation of permeate flux was explained in detail in a study by Shirazi et al. [8]. The flux measurements were done every 10 min after equilibrium was reached and the averaged results were reported. In order to establish a steady state condition for long-time experiments during 15 d, the permeate stream was recycled to the feed storage tank. The repeatability of the permeation flux measurements was found to be at least 90%. Analysis of the saline seawater which was used as feed stream is shown in Table 4. Electrical conductivity meter was used to measure the conductivity of the permeate flow, and the performance of membranes was evaluated based on two major parameters, permeate flux and salt rejection. The resistance boundary layer is very important in laminar flow at low Reynolds numbers [30]. On the feed side, a concentration boundary layer is formed that creates a resistance against the mass transfer. As the feed flow rate increased boundary layer decreased which can be seen in Fig. 6. Also due to the vaporization in the feed side, temperature and concentration polarization affected the flux negatively. One way to offset this effect is to increase the feed flow rate [31]. Higher feed flow rate increased the feed temperature and lowered the partition coefficient (m) between the liquid and gas phase near the membrane. Low partition coefficient resulted in high water concentrations in the membrane and high permeate fluxes correspondingly.

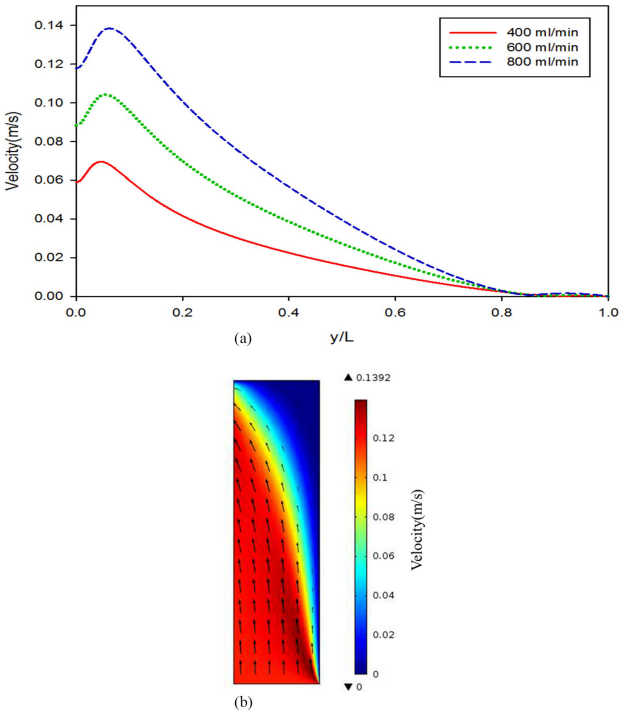

Fig. 5. (a) Velocity profile along the feed side of module at different flow rates (cold stream flow rate = 400 mL/min [0.06 m/s]; T = 80°C). (b) Velocity field in the feed side of the module (feed flow rate = 800 mL/min [0.12 m/s]; T = 80°C).

3.3. Feed temperature

Feed temperature is an important parameter in membrane distillation (MD) performance; it affects vapor pressure of species that transfer through the membrane. MD experiments were carried out at three feed temperature values (50°C, 65°C, and 80°C). The experimental data and simulated results are shown in Figs. 7 and 8. For PTFE membrane, when the feed temperature was increased, the permeate flux increased. The species diffused based on the dissolution–diffusion mechanism from the feed side toward the permeate side through the membrane. When the feed temperature was increased, the pressure difference of the transient species was enhanced throughout the membrane aiding the water molecules to penetrate through membrane's free spaces increasing the permeate flux. Random movement of a polymer chain in the amorphous regions created empty spaces inside the membrane. Therefore, a temperature increase resulted in increased frequency and amplitude of jumping of polymer chains due to increased free spaces inside the membrane [32]. Hence, the diffusion rate of the desired molecules increased as the temperature increased. In addition, the increase in the permeate flux could also be due to the effect of feed on the viscosity and diffusivity of water. When the feed temperature increased, the parameter that was affected significantly in the proposed model was partition coefficient. The compressibility factor of water in the liquid phase (Z_l) increased significantly while the compressibility factor of water in vapor phase (Z_v) decreased slowly. As mentioned earlier, partition coefficient was defined as the ratio of Z_v to Z_l. Thus, low partition coefficient meant high permeate flux. The vapor pressure

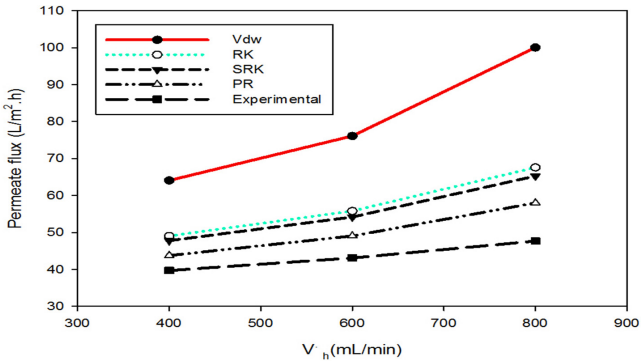

Fig. 6. Effect of feed flow rate on the experimental and simulated flux (cold stream flow rate = 400 mL/min [0.06 m/s]; T = 80°C).

Table 4
Analysis of the saline seawater modeled in this work [8]

Item	Value
Na^+, ppm	14,985
Cl^-, ppm	27,272
SO_4^{2-}, ppm	3,667
Mg^{2+}, ppm	1,940
Ca^{2+}, ppm	1,231
K^+, ppm	581
SiO_2, ppm	0.3
Mn^{2+}, ppm	0.12
Fe^{2+}, ppm	0.054
NH_4^+, ppm	0.05
TSS, ppm	46.7
TDS, ppm	48,000
pH	8.7
Conductivity at 20°C, μS/cm	65,000

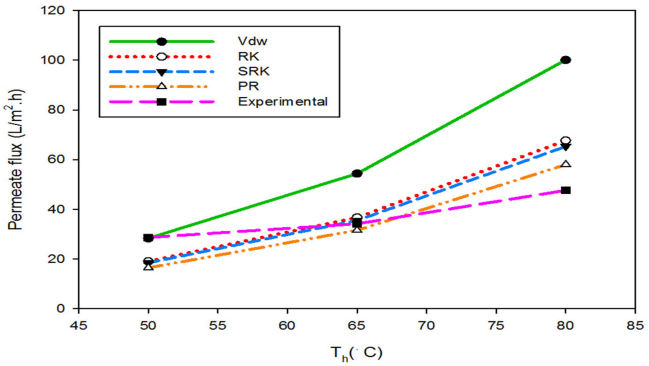

Fig. 7. Effect of feed temperature on the experimental and simulated flux of PTFE membrane (feed flow rate = 800 mL/min; cold stream flow rate = 400 mL/min [0.06 m/s]).

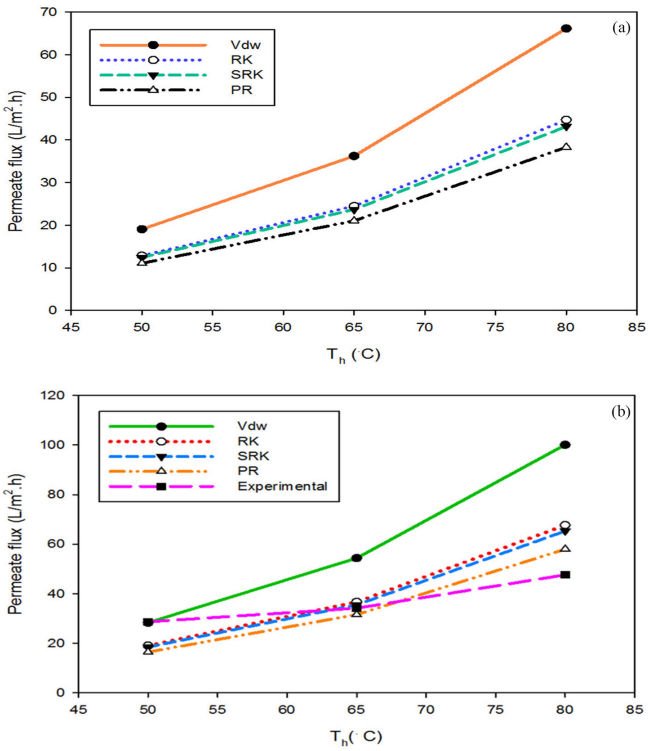

Fig. 8. Effect of feed temperature on the experimental and simulated flux of (a) PVDF membrane and (b) PP membrane (feed flow rate = 800 mL/min [0.12 m/s]; cold stream flow rate = 400 mL/min [0.06 m/s]).

and feed temperature can be related to each other by a well-known equation named Antoine equation. The exponential trend expected from Antoine equation was plotted well based on the modeled data when compared with the experimental data. Deviation between the modeled data and experimental data was higher at high temperatures. This difference can be explained by temperature drop across the membrane which was made by evaporative cooling at the permeate section [33]. Similar trends were reported by other researchers [34–37].

Based on the proposed models, the effects of feed temperature on the permeate flux for PVDF and PP membranes followed a similar trend. In PVDF and PP membranes, the permeate flux was enhanced with the increase in the feed temperature. The PR equation of state revealed the best agreement with the experimental data. The total error of this equation was 0.06%.

3.4. Cold stream flow rate

One of the most effective parameters on membrane performance is cold stream flow rate in DCMD systems. The simulated and experimental results are shown in Fig. 9. Cold stream flow rate was predicted for the PTFE membrane based on the proposed thermodynamic relations and under various operating conditions. Permeate flux increased with an increase in the cold stream flow rate. The increase in the cold stream flow rate increased the pressure difference, thereby increasing permeate flux. In addition, the increase in cold stream rate prevented accumulation of the solute near the permeate side of membrane which may have resulted in reduction of transfer rate from feed side toward permeate side [18]. Moreover, as the cold stream flow rate increased, the temperature and concentration polarization in the permeate section near the membrane decreased. Thus more permeate flux was obtained.

3.5. Flow direction

Among the effective parameters on the permeate flux are feed flow and permeate flow directions. All of the previous results were based on cross-current flow direction in which the majority of the feed flow travels tangentially across the surface of the filter, rather than into the filter. In cross-current flow arrangement, the concentrate feed water flows across the surface of a membrane filter media with minimal solid build-up and at constant low-flow resistance. In this study, co-current and counter-current arrangements were also considered (Fig. 10).

Different flow arrangements were compared (Fig. 11) and cross-counter flow arrangement, which is applied in the experiments, showed highest permeate flux. In this arrangement, the wall acts as a barrier reducing fluid motion and increases residence time of feed inside the membrane, therefore, the transfer rate of solute through the membrane and the permeate flux increases.

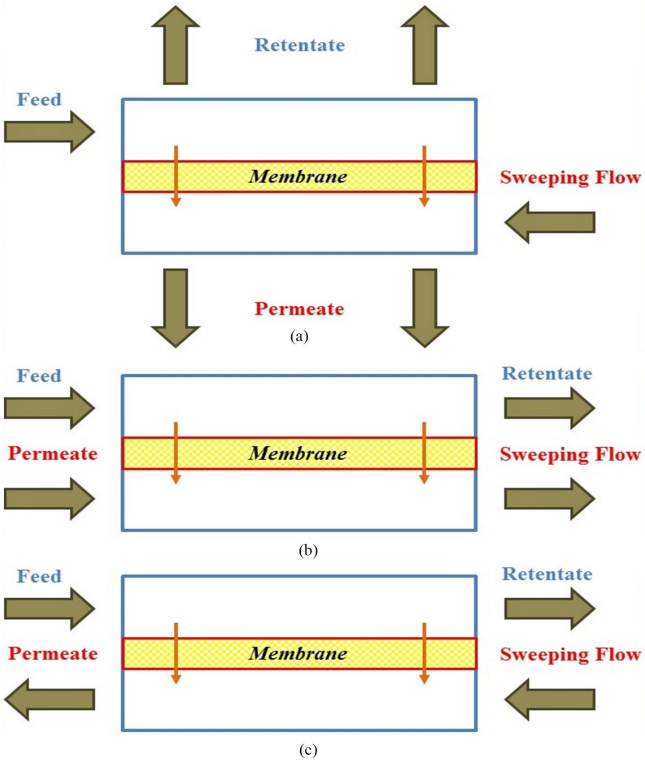

Fig. 10. Different flow rate arrangements in feed and permeate side (a) cross-current, (b) co-current, and (c) counter-current.

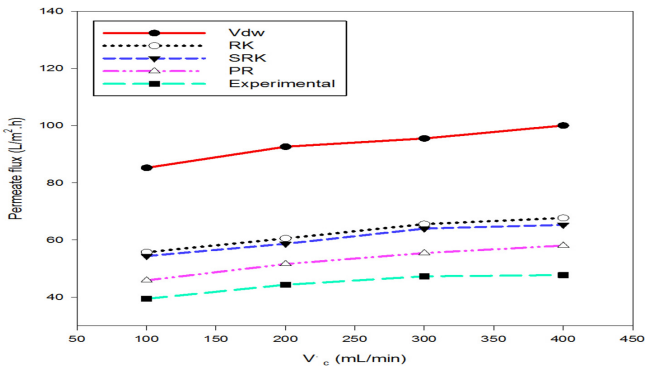

Fig. 9. Effect of cold stream flow rate on the experimental and simulated flux (feed flow rate =800 mL/min [0.12 m/s]; T = 80°C).

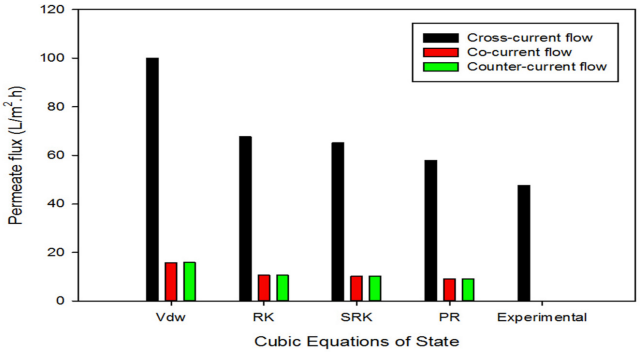

Fig. 11. Effect of flow direction on the experimental and simulated flux using PTFE membrane (feed flow rate = 800 mL/min [0.12 m/s]; T = 80°C; cold stream flow rate = 400 mL/min [0.06 m/s]).

4. Conclusions

A 2D mathematical model was developed to predict the mass and momentum transport of water in PTFE, PP and PVDF membranes. The momentum and continuity equations for water were solved numerically using the finite element method. The effects of feed flow rate, feed temperature, flow direction, and cold stream flow rate on the permeate flux were investigated by CFD and results were compared with experimental data. Based on simulation and experimental results, permeate flux was enhanced as feed temperature, feed flow rate, and permeate flow rate increased. Also, cross-current flow arrangement resulted in higher permeate flux. Using PR equation of state, the model predictions showed better agreement with the experimental data for PTFE, PP, and PVDF membranes in comparison with the other considered thermodynamics generic cubic equations of state.

Symbols

C_W	—	Water concentration, mol/m^3
t	—	Time, s
R_W	—	Chemical reaction, mol/m^3 s
D_W	—	Diffusion coefficient, m^2/s
V	—	Velocity vector, m/s
ρ	—	Density, kg/m^3
P	—	Pressure, Pa
g	—	Gravity, m/s^2
C_{wf}	—	Water concentration in the feed section, mol/m^3
C_{wm}	—	Vapor concentration in the membrane section, mol/m^3
Z_l	—	Water compressibility factor in the liquid phase
Z_v	—	Water compressibility factor in the vapor phase
v	—	Molar volume, 10^{-6} m^3/mole
P	—	Reduced pressure
T_r	—	Reduced temperature
q	—	Dimensionless constant
T	—	Temperature, K
v_l	—	Water molar volume in the liquid phase, 10^{-6} m^3/mole
v_g	—	Water molar volume in the vapor phase, 10^{-6} m^3/mole
A_W	—	Dimensional quantity for water
A_G	—	Dimensional quantity for glucose
B_W	—	Constant
B_G	—	Constant
C_{wp}	—	Vapor concentration in the permeate section, 10^6 mole/m^3
q	—	Mesh quality
A	—	Area, m^2
h_1, h_2, h_3	—	Lengths of the triangular, m

Greek

λ	—	Partition coefficient
μ	—	Dynamic viscosity
β	—	Dimensionless constant
E	—	Dimensionless constant
σ	—	Dimensionless constant
Ω	—	Dimensionless constant
Ψ	—	Dimensionless constant
Ω	—	Acentric factor

References

[1] J. Redondo, Brackish-, sea-and wastewater desalination, Desalination, 138 (2001) 29–40.

[2] T. Kaghazchi, M. Mehri, M.T. Ravanchi, A. Kargari, A mathematical modeling of two industrial seawater desalination plants in the Persian Gulf region, Desalination, 252 (2010) 135–142.

[3] C. Fritzmann, J. Löwenberg, T. Wintgens, T. Melin, State-of-the-art of reverse osmosis desalination, Desalination, 216 (2007) 1–76.

[4] R. Sanders, Water desalting and the Middle East peace process, Technol. Soc., 31 (2009) 94–99.

[5] S. Koushkbaghi, P. Jafari, J. Rabiei, M. Irani, M. Aliabadi, Fabrication of PET/PAN/GO/Fe_3O_4 nanofibrous membrane for the removal of Pb (II) and Cr (VI) ions, Chem. Eng. J., 301 (2016) 42–50.

[6] F. Bozorgpour, H.F. Ramandi, P. Jafari, S. Samadi, S.S. Yazd, M. Aliabadi, Removal of nitrate and phosphate using chitosan/Al_2O_3/Fe_3O_4 composite nanofibrous adsorbent: comparison with chitosan/Al_2O_3/Fe_3O_4 beads, Int. J. Biol. Macromol., 93 (2016) 557–565.

[7] M. Etemadi, S. Samadi, S.S. Yazd, P. Jafari, N. Yousefi, M. Aliabadi, Selective adsorption of Cr (VI) ions from aqueous solutions using Cr^{6+}-imprinted Pebax/chitosan/GO/APTES nanofibrous adsorbent, Int. J. Biol. Macromol., 95 (2017) 725–733.

[8] M.M.A. Shirazi, A. Kargari, M.J.A. Shirazi, Direct contact membrane distillation for seawater desalination, Desal. Wat. Treat., 49 (2012) 368–375.

[9] M. El-Bourawi, Z. Ding, R. Ma, M. Khayet, A framework for better understanding membrane distillation separation process, J. Membr. Sci., 285 (2006) 4–29.

[10] E. Curcio, E. Drioli, Membrane distillation and related operations—a review, Sep. Purif. Rev, 34 (2005) 35–86.

[11] M. Takht Ravanchi, T. Kaghazchi, A. Kargari, Application of membrane separation processes in petrochemical industry: a review, Desalination, 235 (2009) 199–244.

[12] Y.-J. Choi, S. Lee, J. Koo, S.-H. Kim, Evaluation of economic feasibility of reverse osmosis and membrane distillation hybrid system for desalination, Desal. Wat. Treat., 57 (2016) 24662–24673.

[13] A.M. Alklaibi, N. Lior, Membrane-distillation desalination: status and potential, Desalination, 171 (2005) 111–131.

[14] H.C. Duong, A.R. Chivas, B. Nelemans, M. Duke, S. Gray, T.Y. Cath, L.D. Nghiem, Treatment of RO brine from CSG produced water by spiral-wound air gap membrane distillation — a pilot study, Desalination, 366 (2015) 121–129.

[15] C.R. Martinetti, A.E. Childress, T.Y. Cath, High recovery of concentrated RO brines using forward osmosis and membrane distillation, J. Membr. Sci., 331 (2009) 31–39.

[16] L.D. Nghiem, F. Hildinger, F.I. Hai, T. Cath, Treatment of saline aqueous solutions using direct contact membrane distillation, Desal. Wat. Treat., 32 (2011) 234–241.

[17] F. Laganà, G. Barbieri, E. Drioli, Direct contact membrane distillation: modelling and concentration experiments, J. Membr. Sci., 166 (2000) 1–11.

[18] K. Charfi, M. Khayet, M. Safi, Numerical simulation and experimental studies on heat and mass transfer using sweeping gas membrane distillation, Desalination, 259 (2010) 84–96.

[19] Z. Xu, Y. Pan, Y. Yu, CFD simulation on membrane distillation of NaCl solution, Front. Chem. Eng. China, 3 (2009) 293–297.

[20] N. Tang, H. Zhang, W. Wang, Computational fluid dynamics numerical simulation of vacuum membrane distillation for aqueous NaCl solution, Desalination, 274 (2011) 120–129.

[21] H. Yu, X. Yang, R. Wang, A.G. Fane, Numerical simulation of heat and mass transfer in direct membrane distillation in

a hollow fiber module with laminar flow, J. Membr. Sci., 384 (2011) 107–116.
[22] M. Hasanizadeh, P. Jafari, B. Farshighazani, M.K. Moraveji, CFD simulation of heat and mass transport for water transfer through hydrophilic membrane in direct-contact membrane distillation process, Desal. Wat. Treat., 57 (2016) 18109–18119.
[23] P. Jafari, M. Keshavarz Moraveji, Application of generic cubic equations of state in the CFD simulation of the sweeping gas polytetrafluoroethylene (PTFE) membrane distillation, Desal. Wat. Treat., 57 (2016) 1647–1658.
[24] R.B. Bird, W.E. Stewart, E.N. Lightfoot, Transport Phenomena, Wiley & Sons, 2007.
[25] C. Wilke, P. Chang, Correlation of diffusion coefficients in dilute solutions, AIChE J., 1 (1955) 264–270.
[26] J.H. Perry, Chemical engineers' handbook, J. Chem. Educ., 27 (1950) 533.
[27] J.M. Smith, H.V. Ness, Introduction to Chemical Engineering Thermodynamics, McGraw-Hill: New York, 2011.
[28] P.M. Shehni, A.E. Amooghin, A. Ghadimi, M. Sadrzadeh, T. Mohammadi, Modeling of unsteady-state permeation of gas mixture through a self-synthesized PDMS membranes, Sep. Purif. Technol., 76 (2011) 385–399.
[29] A. Alkhudhiri, N. Darwish, N. Hilal, Membrane distillation: a comprehensive review, Desalination, 287 (2012) 2–18.
[30] M. She, S.-T. Hwang, Concentration of dilute flavor compounds by pervaporation: permeate pressure effect and boundary layer resistance modeling, J. Membr. Sci., 236 (2004) 193–202.
[31] M. Khayet, Membranes and theoretical modeling of membrane distillation: a review, Adv. Colloid Interface Sci., 164 (2011) 56–88.
[32] B. Smitha, D. Suhanya, S. Sridhar, M. Ramakrishna, Separation of organic–organic mixtures by pervaporation—a review, J. Membr. Sci., 241 (2004) 1–21.
[33] D. O'Brien, J. Craig, Jr, Ethanol production in a continuous fermentation/membrane pervaporation system, Appl. Microbiol. Biotechnol., 44 (1996) 699–704.
[34] M.D. Mobarake, P. Jafari, M. Irani, Preparation of Pd-based membranes on Pd/TiO_2 modified NaX/PSS substrate for hydrogen separation: design and optimization, Microporous Mesoporous Mater., 226 (2016) 369–377.
[35] A. Khalifa, D. Lawal, M. Antar, M. Khayet, Experimental and theoretical investigation on water desalination using air gap membrane distillation, Desalination, 376 (2015) 94–108.
[36] Y.M. Manawi, M.A. Khraisheh, A.K. Fard, F. Benyahia, S. Adham, A predictive model for the assessment of the temperature polarization effect in direct contact membrane distillation desalination of high salinity feed, Desalination, 341 (2014) 38–49.
[37] S. Samadi, S.S. Yazd, H. Abdoli, P. Jafari, M. Aliabadi, Fabrication of novel chitosan/PAN/magnetic ZSM-5 zeolite coated sponges for absorption of oil from water surfaces, Int. J. Biol. Macromol., 105 (2017) 370–376.